A Joint Suppression Method of Scalloping and Inter-Scan Banding for SAR Images

Xinwei An, *Graduate Student Member, IEEE*, Wei Yang, *Member, IEEE*, Haijun Shen, Hongcheng Zeng, *Member, IEEE*, Fei Zou, Jiadong Deng, *Graduate Student Member, IEEE*, Can Su, *Graduate Student Member, IEEE*, and Wei Liu, *Senior Member, IEEE*

***Abstract*—Due to a wide swath at the order of hundreds of kilometres, interscan banding (ISB) may occur in both ScanSAR and TOPS modes of a synthetic aperture radar (SAR), leading to degraded image quality. In this aticle, the causes of ISB are analyzed and an ISB suppression method based on Retinex theory and global weighting is proposed. First, the image with ISB is considered as an image with uneven lighting, and ISB is considered as a lighting component. The ISB component is calculated using a global weighting method. Based on previous studies, the coupling relationship between ISB and scalloping (another issue commonly found in ScanSAR) is identified, and a joint procedure for suppressing ISB and scalloping is established. The proposed method is a post-processing technique that does not require any other additional information, such as the noise equivalent sigma zero. Experimental results based on real SAR images from Gaofen-3 and Sentinel-1 indicate that the proposed method can significantly reduce the effect of ISB and improve the image quality, and it is more efficient and robust compared to existing methods.**

***Index Terms*—Gaofen-3 (GF-3), interscan banding (ISB) suppression, ScanSAR, Sentinel-1, TOPSAR.**

I. INTRODUCTION

SYNTHETIC aperture radar (SAR) can acquire high-resolution remote sensing images of ground scenes regardless of weather and lighting conditions, and has been widely used in various fields, including military and civilian applications [1]. It has several operating modes including StripMap, SpotLight, Sliding Spotlight, ScanSAR, and TOPS. The images produced by ScanSAR and TOPS modes normally have a swath width of several hundred kilometres. ScanSAR has the capability to adjust the angle of the antenna during operation, allowing for the scanning of multiple subswaths to obtain a larger mapping band. However, due to the shape of the azimuth antenna pattern (AAP), targets located in different azimuth positions will have different amplitude weights, resulting in periodic light and dark stripes in the image, also known as the scalloping effect. In order to solve the problem of scalloping, TOPSAR was developed [2]. In TOPS mode, the SAR beam is scanned repeatedly along the azimuthal direction, which theoretically can effectively avoid scalloping. However, in the case of multiple subswaths, in the range direction, both ScanSAR and TOPS modes often exhibit drastic pixel intensity variations, referred to as interscan banding (ISB), which is particularly noticeable at the boundaries of different subswaths. In some studies, ISB and scalloping are also collectively referred to as thermal noise [3]. The cause of ISB is the mismatch between the range antenna pattern and the actual image. ISB and scalloping significantly degrades the quality of SAR images, which makes it difficult for subsequent processing, such as sea-ice detection, ship detection, and sea surface wind speed retrieval [4], [5], [6]. Moreover, in ship navigation, the presence of scalloping and ISB may lead to misjudgment of ship positions and potential hazards, while in coastal monitoring, it can affect the accurate detection of coastline changes and small structures. Therefore, ISB and scalloping suppression is crucial for the development of SAR technology. In parallel with the efforts in suppressing ISB and scalloping, other advanced techniques in the SAR research community have also been evolving. For instance, the active multitarget domain adaptation strategy has been making strides in enhancing the adaptability of models across different domains, while the multikernel-size feature fusion-based CNN has shown great potential in improving the feature extraction and classification accuracy [7], [8], [9], [10].

Because the causes for them are independent of each other, most existing studies on the suppression of ISB and scalloping have been conducted separately. The earlier ISB suppression studies focused on the noise equivalent sigma zero (NESZ), which can be regarded as additive noise on SAR images, and were mostly on TOPSAR images from Sentinel-1. Sentinel-1 was developed and completed by the European Space Agency (ESA) and provides researchers with a large amount of free and open-source SAR data, of which NESZ is documented in the metadata [11]. The SAR images provided by ESA have been processed, but they still have many flaws and are not directly usable. Park et al. [3] proposed an empirical optimization-based method for building a noise field to find the noise scaling factor

Received 9 October 2024; revised 17 January 2025 and 25 January 2025; accepted 14 February 2025. Date of publication 18 February 2025; date of current version 7 March 2025. This work was supported by the National Natural Science Foundation of China under Grant 62101014 and 62271028. *(Corresponding author: Hongcheng Zeng.)*

Xinwei An, Wei Yang, Hongcheng Zeng, Jiadong Deng, and Can Su are with the School of Electronic and Information Engineering, Beihang University, Beijing 100191, China (e-mail: anxinwei@buaa.edu.cn; yang-weigigi@sina.com; zenghongcheng@buaa.edu.cn; djdong0725@buaa.edu.cn; can_su@buaa.edu.cn).

Haijun Shen is with the Shanghai Institute of Satellite Engineering, Shanghai 200240, China (e-mail: shenhaijun1987@126.com).

Fei Zou is with the Beijing Institute of Remote Sensing Information, Beijing 100192, China (e-mail: z_feifei@126.com).

Wei Liu is with the Department of Electrical and Electronic Engineering, The Hong Kong Polytechnic University, Hong Kong (e-mail: w.liu@qmul.ac.uk).

Digital Object Identifier 10.1109/JSTARS.2025.3543356

© 2025 The Authors. This work is licensed under a Creative Commons Attribution 4.0 License. For more information, see https://creativecommons.org/licenses/by/4.0/

for NESZ of each subswath separately. However, this method requires a certain number of images for pre-training and the noise scaling factor is a fixed value, which makes it less applicable for images from other satellites. Korosov et al. [12] improved the algorithm by taking into account the shift of the noise vector in the range and analyzed images with different acquisition mode (EW, IW) and different polarization modes (HV, VH). Lee et al. [13] proposed a quadratic function to model the characteristics of the estimated noise field in TOPSAR cross-polarized images. The method does not require a pretrained dataset and can provide dynamic scaling parameter estimates for each image adaptively. Lee et al. [14] established a noise model that transforms ISB into a geometric planning problem, which solves the problem of nonlinear misalignment of NESZ with the real image. All of the methods mentioned above can utilize NESZ to suppress ISB and enhance the quality of SAR images. However, a major shortcoming is that NESZ may be not available in all SAR image products. Even when it is provided, if there are inaccuracies or errors in the NESZ values, the effectiveness of ISB suppression will be significantly compromised. Therefore, an ISB suppression method without the need of NESZ is required. Iqbal and Chen [15] proposed a Kalman filter-based method to suppress scalloping and ISB in ScanSAR images. Nevertheless, it suffers from several limitations. Specifically, the Kalman filter approach requires sequential iterative computations of the ISB components for each corresponding column in every range. This process demands substantial computational resources and is time-consuming, often posing a significant burden in practical applications where efficiency is crucial. Moreover, its specialty lies in being primarily devised to handle periodic patterns like scalloping. However, when dealing with ISB, which typically exhibits non-periodic and random characteristics, the performance of Kalman filter is quite limited, as it fails to adapt well to the unpredictable nature of ISB. Consequently, further research and efforts are necessary to develop more effective means of suppressing ISB and enhancing the overall quality of SAR image processing.

In this article, a joint suppression method for scalloping and ISB is proposed without additional information. The proposed method is suitable for amplitude or intensity images of level 1 products. In Section II, the causes of scalloping and ISB are analyzed. Referring to the Retinex theory, images with ISB are considered as having uneven illumination, and a global weighting method is used to calculate the ISB component, which is then formed as the basis for ISB suppression. Based on the previous work, a joint procedure for ISB and scalloping suppression, which could adopt different processes based on the specific image, is established. In Section III, three experiments are carried out to validate the proposed method. The first experiment simulates the scalloping and ISB effect of Sentinel-1 and Gaofen-3 (GF-3) on resultant images, which are used to evaluate the performance of the proposed method for image quality enhancement; the second experiment performs ISB suppression on real SAR images of GF-3 and Sentinel-1; and the third experiment provides a discussion on the computational efficiency of the proposed method and its ability to retain image targets. The first two experiments demonstrate that the proposed method can effectively suppress ISB for SAR images from different satellites, resulting in significant improvement in image quality, while the third one shows that the proposed method is more efficient and better at retaining target details than the method based on Kalman filter. Finally, Section IV concludes this article.

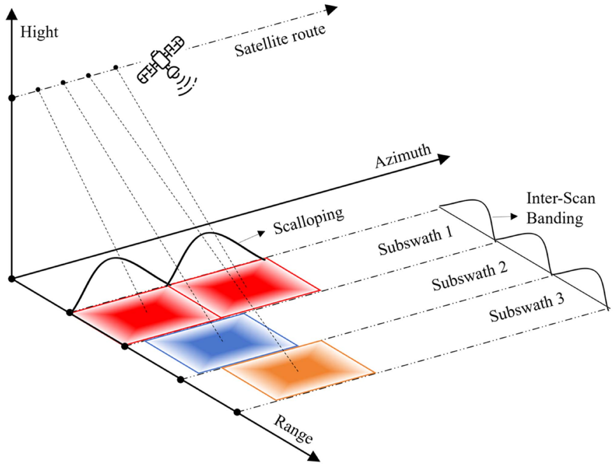

Fig. 1. ScanSAR acquisition geometry.

II. METHODOLOGY

A. Causes of Scalloping

ScanSAR scans multiple subswaths by changing the pointing direction of its antenna, with the aim of obtaining a wider mapping width. Starting from the first subswath, after scanning the current subswath within a short time interval, the antenna changes its attitude and scans the next one. The operating mode of ScanSAR is shown in Fig. 1. Since the target in ScanSAR is illuminated by different parts of the AAP, the radiation characteristics change periodically in the azimuth, also known as scalloping.

The working mechanism of TOPSAR is similar to that of ScanSAR, but the beam of TOPSAR rotates slowly and uniformly in the azimuth, so that the target is weighted by the AAP to the same degree. The operating mode of TOPSAR is shown in Fig. 2. In terms of the imaging mechanism, TOPSAR can effectively avoid scalloping, which is why a large number of satellites adopted the mode as soon as it was proposed. However, due to errors, such as in antenna scanning, an amplitude modulation error similar to scalloping may appear in TOPSAR images, most notably in Sentinel-1 images [3]. For ease of processing, this can be summarized as scalloping. Although the behavior is very similar, the reasons for the scalloping of TOPSAR are quite different from those in ScanSAR. In TOPS mode, when the phased array antenna controls the steering of the azimuthal beam, slight scalloping occurs due to the reduction in the main lobe gain. Scalloping becomes more obvious as the azimuth angle increases [19]. In the current SAR satellites, such as GF-3, there is no obvious scalloping effect in the TOPSAR image [6], thanks to advanced hardware equipment and imaging technology.

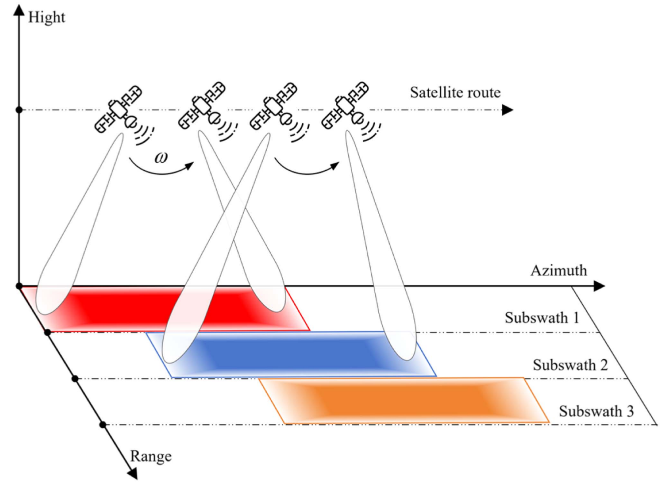

Fig. 2. TOPSAR acquisition geometry.

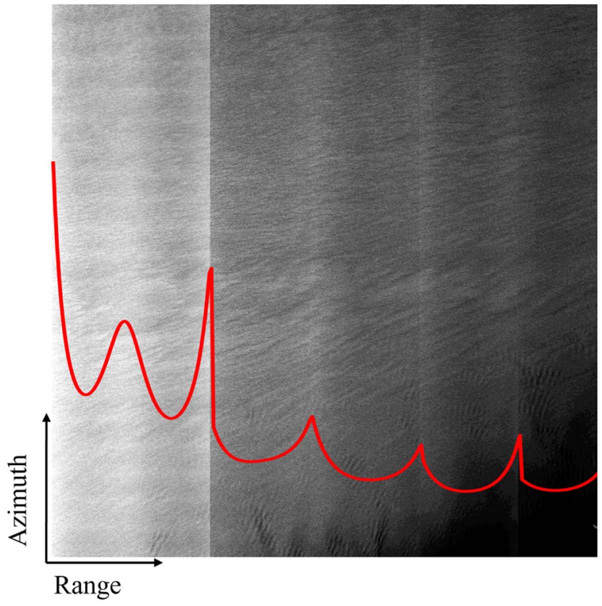

Fig. 3. TOPSAR image with interscan banding from Sentinel-1, where the red curve represents the NESZ curve of the image.

In a word, scalloping in ScanSAR is an unavoidable flaw inherent in its model design. By contrast, the scalloping problem in TOPSAR is an imperfection in the design of the system that can be avoided [20], [21].

B. Causes of Interscan Banding

While the TOPS mode effectively eliminates scalloping in the azimuth, it does not address the issue of ISB in the range. This problem also exists in the ScanSAR mode. ISB is a problem caused by switching the antenna beam in different subswaths, resulting in nonperiodic random noise in the SAR image in the range direction. As shown in Fig. 3, the NESZ of each subswath exhibits a fluctuating state within the subswath and a step state at the subswath's boundary. For the antenna gain pattern in the range, the deviations could be categorized into two types: lateral deviation and vertical deviation.

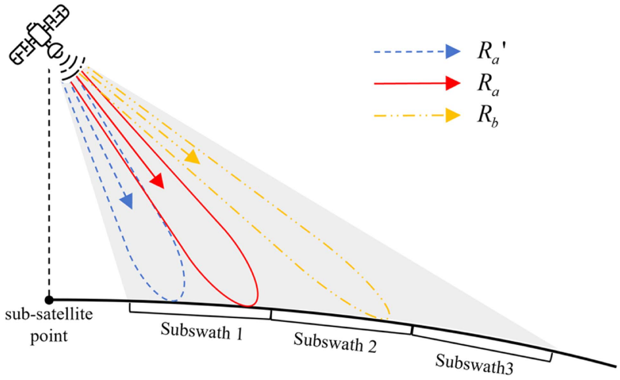

Fig. 4. Source analysis of interscan banding.

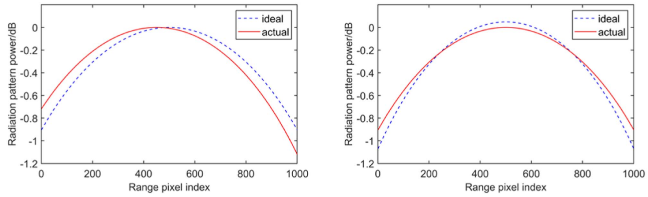

(a) (b)

Fig. 5. Error of antenna gain pattern. (a) Lateral deviation. (b) Vertical deviation.

The presence of horizontal and vertical deviations helps explain the irregular manifestations of ISB across different subswaths. In the SAR imaging process, each subswath's antenna pattern is independently computed. The lateral and vertical deviations within each subswath are mutually independent. This independence leads to the step changes between subswaths and the fluctuation variations within each subswath observed in the entire image. This complex combination of independent deviations in different subswaths ultimately gives rise to the highly variable and irregular ISB in the SAR image. Below is a detailed analysis of the causes of lateral and longitudinal errors.

Lateral deviations may be caused by the beam pointing error [22]. Various factors in space and the satellite's own motion can cause the roll angle to wobble, resulting in beam pointing error in the range. This manifests as a shift in the beam coverage area, as shown in Fig. 4. The real irradiated beam is denoted as R_a (red solid beam), while the system mistakenly believes the irradiated beam to be R_a' (blue dashed beam). The radar may encounter issues in receiving echo for imaging due to radiation bias, which is demonstrated by the antenna gain pattern in Fig. 5(a). The blue dashed line represents the system's ideal beam pointing, while the red solid line represents the actual beam pointing. Fig. 6(a) shows that the image will have uneven ISB gain due to lateral deviation, resulting in unidirectional brightness variations. The ISB gain in Fig. 6 is obtained by calculating the ratio of the actual antenna gain which is affected by the lateral deviation to the ideal antenna gain.

The source of vertical deviation is a little complex and can be caused by incorrect antenna compensation [23]. The relationship

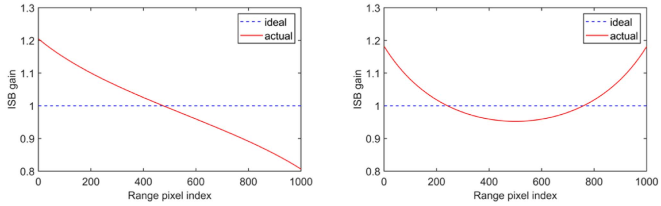

(a) (b)

Fig. 6. Error of ISB gain. (a) Lateral deviation. (b) Vertical deviation.

between radar echo power and distance between target and radar can be described using the radar equation

$$P_r = \frac{P_t G^2 \lambda^2 \sigma}{L_n (4\pi)^3 R^4} \tag{1}$$

where P_r is echo power received by the radar, P_t is radar transmit power, G is antenna gain, λ is wavelength of the electromagnetic wave, σ is radar cross section, L_n is the system loss, and R is the distance between target and radar.

According to (1), the echo power decreases as the fourth power of the distance, resulting in greater energy attenuation for long-range targets. To compensate for this effect, the radar will set the antenna gain in the long-range area to be larger, so the radar does not have a consistent weighting of the beam in the range. However, it may not compensate the antenna gain accurately, resulting in either overcompensation or undercompensation. This, in turn, causes vertical deviation in the echo energy received, as shown in Fig. 5(b). The blue dashed line represents the system's ideal estimation, while the red solid line represents the actual situation. The vertical deviation of the antenna pattern can cause an uneven ISB gain in the image, as shown in Fig. 6(b). It manifests on the image's gray curve as a change shaped like a "*u*" or "*n*." Specifically, for the "*u*" shaped brightness change, it indicates that the brightness is higher in the middle region of the gray curve and gradually decreases towards both ends. For the "*n*" shaped brightness change, it means that the brightness is lower in the middle region of the gray curve and gradually increases at both ends.

Earth is not a standard sphere, and even for circular orbits, the height of the target is constantly changing. When the actual and expected directions of arrival of the signal mismatch with each other due to unmodeled terrain height and pulse duration, deviations would occur in the antenna pattern [24], [25]. As shown in Fig. 4, when the beam R_b with a large incidence angle is directed towards the ground, the curvature of the earth causes some deviation in the beam radiation region, which, together with the nonuniform antenna gain compensation, results in severe ISB on the image. As it is impossible to estimate the bias, the ISB is highly variable, which is consistent across both ScanSAR and TOPS modes.

C. Suppression Model of Scalloping and Interscan Banding

Since ISB and scalloping have different causes, they can be treated as independent of each other and modeled separately for suppression, ultimately improving image quality.

Scalloping exhibits a regular periodic distribution with a relatively small magnitude of variation compared to the image intensity. This makes it suitable for processing by Kalman filter with the concept of local correction, where scalloping is considered as additive noise to the image, with a periodic distribution in the azimuth and fixed in the range [18], with the following model:

$$I_1(x, y) = I_0(x, y) + N_a(x) \tag{2}$$

where I_0 represents the ideal SAR image, while I_1 is the SAR image with scalloping. The variables (x, y) represent the coordinates of the pixels, where x is the azimuth direction and y is the range direction. Additionally, $N_a(x)$ represents the additive noise distributed along the azimuth direction and corresponds to the scalloping. Obviously, this model is only applicable to suppressing scalloping for images where ISB is not significant. Due to the randomness and significant bias of ISB, the method based on Kalman filter is not suitable for ISB suppression. Therefore, it is necessary to explore alternative theories for modelling ISB.

The SAR image with ISB is similar to a grey-scale image with uneven light distribution. Referring to the Retinex theory, an image can be represented as the product of two components: the illumination component and the reflection component. The reflection component contains the essential information of the scene, while the illumination component is the interference to the image caused by the light source and environmental factors. Likewise, the SAR image can be regarded as a combination of the ideal SAR image and the multiplicative noise. The former corresponds to the reflection component, while the latter corresponds to the illumination component. The following model is constructed:

$$I_1(x, y) = I_0(x, y) \times N_r(y) \tag{3}$$

where $N_r(y)$ denotes the multiplicative noise associated with the SAR image [26]. Specifically, ISB is modeled as a multiplicative noise that is distributed along the range direction with a constant value in the azimuth. Our objective is to isolate the ISB component from the original SAR image.

In order to facilitate the computation and reduce the complexity of the algorithm, (3) is transformed into the logarithmic domain

$$\log\left[I_1(x, y)\right] = \log\left[I_0(x, y)\right] + \log\left[N_r(y)\right]. \tag{4}$$

In other papers that utilize Retinex theory to enhance image quality, Gaussian kernel convolution is commonly used to identify the light component of the image. However, this method is not suitable here due to the randomness and one-dimensionality of the ISB. Different from the Kalman filter-based approach which has limitations, such as high computational complexity and poor adaptability to the randomness of ISB, our proposed modeling method can break free from these limitations. It can reduce computational complexity and achieve adaptive processing of random ISB. In our proposed method, the ISB and the true value of the image could be considered as the estimated value and the background noise, respectively. The global weighting-based ISB component estimation model is established by taking the

Algorithm 1: Suppress Scalloping and ISB on TOPSAR Images.

```
/* $I$ is the original image, and $s$ is subswath from $I$ */
for each subswath $s(x, y) \in I(x, y)$ do
    /* ISB suppression */
    Turn $s(x, y)$ to the logarithmic domain as $log\_s(x, y)$;
    $m(y) \leftarrow$ mean value of $log\_s(x, y)$ in the azimuth;
    $\alpha \leftarrow$ mean value of $log\_s(x, y)$;
    $c(y) \leftarrow m(y) - \alpha$;
    /* $c$ is the correction factor */
    $T(x, y) \leftarrow log\_s(x, y) - c(y)$ in each azimuth;
    Turn $T$ to spatial domain as $s'$;
    /* $s'$ is the subswath after ISB suppression */
    for $s'$, suppress scalloping in [18], get $s''$;
    /* $s''$ is the subswath after scalloping suppression */
end
$I' \leftarrow$ Splice $s''$ together;
/* $I'$ is the image spliced by subswath $s''$ */
Perform ISB suppression on $I'$ to obtain $I''$;
/* $I''$ is the final image after scalloping and ISB suppression */
```

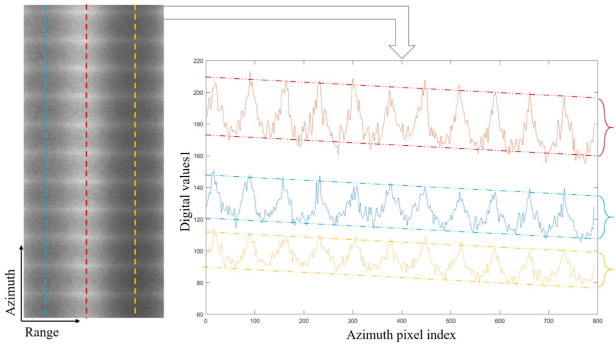

Fig. 7. Left image is a stable sea area captured by Sentinel-1; a series of pixel intensities at the positions of the blue, red, and yellow dashed lines are represented in the image on the right, which shows difference in the intensity of scalloping at different azimuth positions.

pixel mean value of the whole image as the reference standard and the pixel weight of the image in the range as the ISB

$$\log\left[N_r(y)\right] = \sum_{i=1}^{m} \log\left[I_1(i, y)\right] - \frac{1}{n} \sum_{j=1}^{n} \sum_{i=1}^{m} \log\left[I_1(i, j)\right] \quad (5)$$

where m denotes the number of pixels in the SAR image in the azimuth direction and n denotes the number of pixels in the range. The obtained noise component is subtracted from the original image in the logarithmic domain and undergoes another logarithmic transformation to obtain the target image I_0, the image after ISB suppression

$$I_0(x, y) = \exp\left\{\log\left[I_1(x, y)\right] - \log\left[N_r(y)\right]\right\}. \quad (6)$$

Although scalloping and ISB have been modeled separately and independent of each other, it is necessary to consider a sequential order of treatment to identify their coupling relationship. Fig. 7 displays an image of a stable sea with scalloping and ISB from Sentinel-1. Three sets of data at different range positions are selected and marked with blue, red, and yellow lines. The red line is in the bright part of the image, the blue line is in the relatively dark part, and the yellow line is in the area with the deepest degree of shading. The data for the three lines is displayed along the azimuth, revealing varying scalloping fluctuations in different regions. The pixel float values are 22.6, 27.9, and 37.2, respectively, indicating that scalloping is influenced by ISB. Therefore, the coupling between them can be determined by building the following joint model:

$$I_1(x, y) = \left[I_0(x, y) + N_a(x)\right] \times N_r(y). \quad (7)$$

The first step is to suppress ISB, followed by scalloping, and the detailed process is described in the following section.

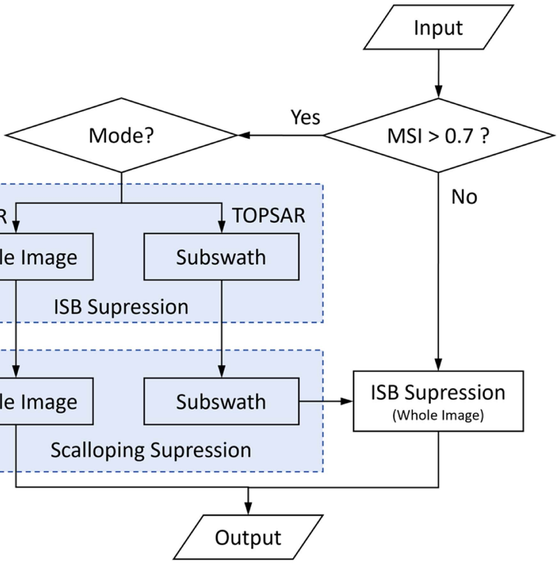

Fig. 8. Flowchart of the proposed procedure.

D. Removal of Scalloping and Interscan Banding

Due to differences in scanning methods, there is a degree of variation between ScanSAR and TOPSAR in suppressing scalloping and ISB. This will be analyzed as follows.

For TOPSAR images that exhibit both scalloping and ISB, it is recommended to first perform ISB suppression and scalloping suppression in the subswaths, followed by ISB suppression in the whole image. The overall process for TOPSAR images with scalloping and ISB is given in Algorithm 1. ISB suppression is performed on the whole image due to two considerations. First, different subswaths have energy bias, which needs to be compensated by ISB suppression in the whole image. Second, the suppression of scalloping may lead to reappearance of clear dividing lines between subswaths. It is worth mentioning that the subswaths of TOPSAR have the same scalloping width generally, but scalloping between subswaths is not constant in the range. Figuratively speaking, scalloping on different subswaths can be misaligned, which is more intuitively shown in Section III.

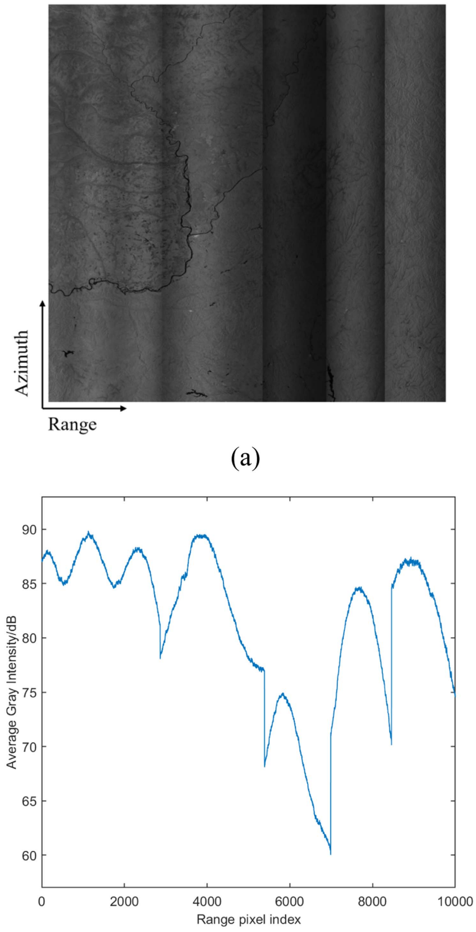

(a)

(b)

Fig. 9. (a) ScanSAR image with interscan banding from Gaofen-3. (b) Average gray intensity (AGI) of the image in the range.

ScanSAR does not suffer from this problem, so ISB suppression and scalloping suppression can be applied to the whole ScanSAR image. If there is no obvious scalloping effect in the SAR image, then ISB suppression can be performed directly. Mean scalloping intensity (MSI) is chosen as the basis for evaluating the degree of scalloping effect, as explained in detail in the following subsection. In this article, a comprehensive procedure for scalloping and ISB suppression is developed as shown in Fig. 8.

E. Quantitative Expression

In order to quantify the performance of the proposed method on ISB suppression, the average gray intensity index (AGI) is introduced [18], as defined in the following equation:

$$\mathrm{AGI}(y) = 20 \cdot \log\left[\frac{1}{m}\sum_{x=1}^{m} I(x,y)\right]. \tag{8}$$

Fig. 9(a) shows a SAR image with ISB, and Fig. 9(b) shows the corresponding AGI curve. The energy fluctuation of the SAR image in the range can be visualized on the image, but there is still a lack of a metric to measure it. Therefore, we propose a new index called the degree of range fluctuation (DRF), which is defined as the pixel fluctuation of the SAR image in the range. The larger the value, the larger the ISB in the image, with the following formula:

$$\mathrm{DRF} = \sqrt{\frac{\sum_{y=1}^{n}\left(\mathrm{AGI}(y)-\mu\right)^2}{n}} \tag{9}$$

where μ is the mean value of the AGI curve of the SAR image

$$\mu = \frac{1}{n}\sum_{y=1}^{n}\mathrm{AGI}\,(y). \tag{10}$$

Both local scalloping intensity (LSI) and MSI introduced in [18] are used as a basis for judging the scalloping level

$$\mathrm{LSI}(x) = 20\,\mathrm{lg}\left\{\frac{\max\left[\frac{1}{n}\sum_{y=1}^{n} I(x,y)\right]_{\text{local}}}{\min\left[\frac{1}{n}\sum_{y=1}^{n} I(x,y)\right]_{\text{local}}}\right\} \tag{11}$$

$$\mathrm{MSI} = \frac{1}{m}\sum_{x=1}^{m}\mathrm{LSI}(x). \tag{12}$$

Based on results of numerous experiments, $\mathrm{MSI} = 0.7$ dB is chosen as the threshold: a value larger than 0.7 dB indicates an images with significant scalloping and scalloping suppression is then performed on it. For TOPSAR images, considering the impact of ISB in the whole image, the first subswath will be selected to calculate its MSI.

III. EXPERIMENTS

In order to verify the effectiveness of the proposed ISB suppression method, three experiments are carried out for evaluation. The first experiment selects a set of SAR images as a reference, to which scalloping and ISB are added as experimental objects; in the second experiment, a real SAR image with ISB is used, including two scanning modes, ScanSAR and TOPS; and the third experiment is to verify the retention ability of the proposed method for image targets by comparing the image details, and the computational efficiency of the proposed method is also discussed. In this section, the simulated images are from ICEYE satellite, ScanSAR images are from GF-3, and TOPSAR images are from Sentinel-1, and the experimental method used for comparison is the method based on Kalman filter in [15].

A. Scalloping and Interscan Banding Suppression of Simulated Images

Three high-quality TOPSAR images from the ICEYE satellite are selected to add scalloping and ISB. Specifically, for generating the TOPSAR's scalloping and ISB similar to those in Sentinel-1's EW and IW scanning modes, we adopt the method described in [13]. This method commences by identifying a stable background area, preferably an ocean scene. The range gray-scale variation in such a scene is relatively stable and consistent, making it an ideal candidate for a template SAR noise field. Subsequently, through the adjustment of specific

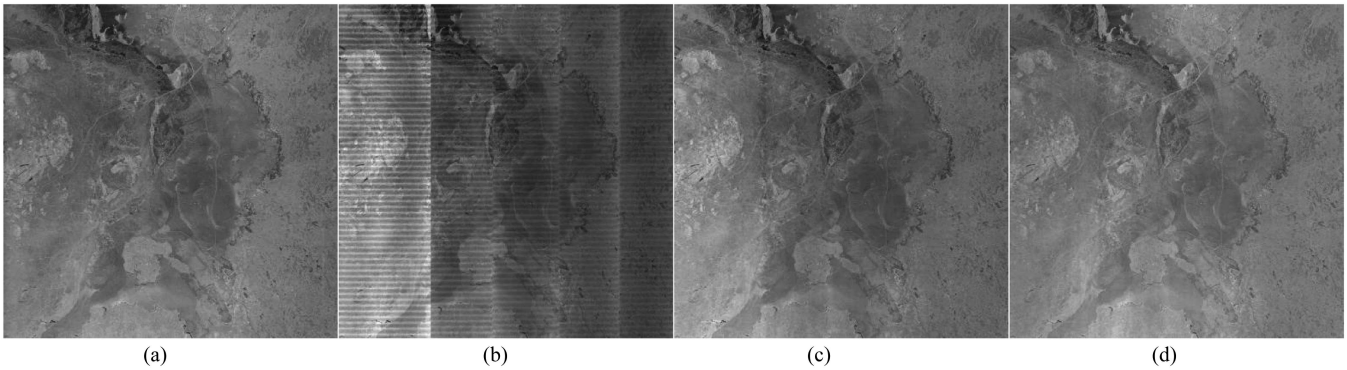
(a) (b) (c) (d)

Fig. 10. Simulated EW correction comparison (data ID: ICEYE_GRD_SC_247678_20220306T100731). (a) original image. (b) Noisy image. (c) Kalman filter. (d) Proposed method.

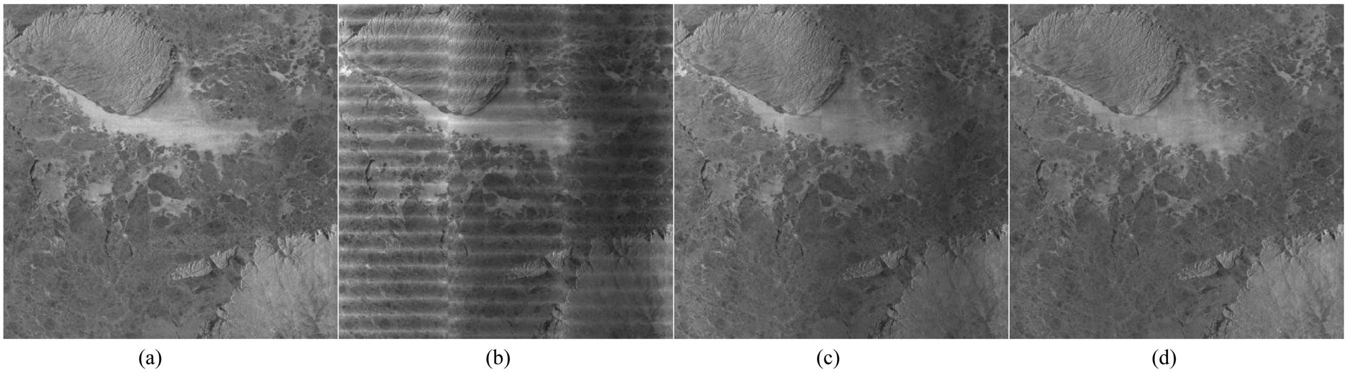
(a) (b) (c) (d)

Fig. 11. Simulated IW correction comparison (data ID: ICEYE_GRD_SC_250939_20220213T160028). (a) Original image. (b) Noisy image. (c) Kalman filter. (d) Proposed method.

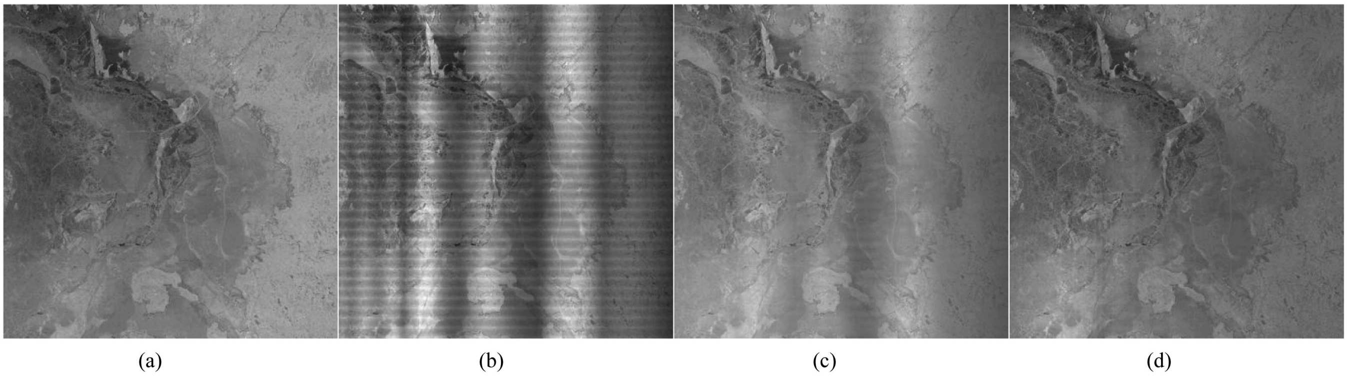
(a) (b) (c) (d)

Fig. 12. Simulated ScanSAR correction comparison (data ID: ICEYE_GRD_SC_247683_20220225T181901). (a) Original image. (b) Noisy image. (c) Kalman filter. (d) Proposed method.

coefficients and multiplying them with the original image, an image with simulated noise is obtained. Regarding the generation of scalloping and ISB, we draw references from the actual image characteristics of GF-3 and Sentinel-1. By meticulously analyzing the typical patterns of scalloping and ISB present in these images, we utilize mathematical models to simulate and incorporate similar effects into the selected ICEYE satellite images. During this process, the imaging parameters and antenna patterns unique to ScanSAR are taken into account to ensure the fidelity of the added noise. The experimental results are shown in Figs. 10–12. The MSI of these three images is 3.30, 3.02, and 1.60, respectively, so scalloping suppression is required for all of them. In addition, the method for suppressing scalloping is the one proposed in [18].

In order to quantify the results, in addition to the DRF proposed in this article, we select two additional metrics for evaluation; the structural similarity index measure (SSIM) and the peak signal-to-noise ratio (PSNR).

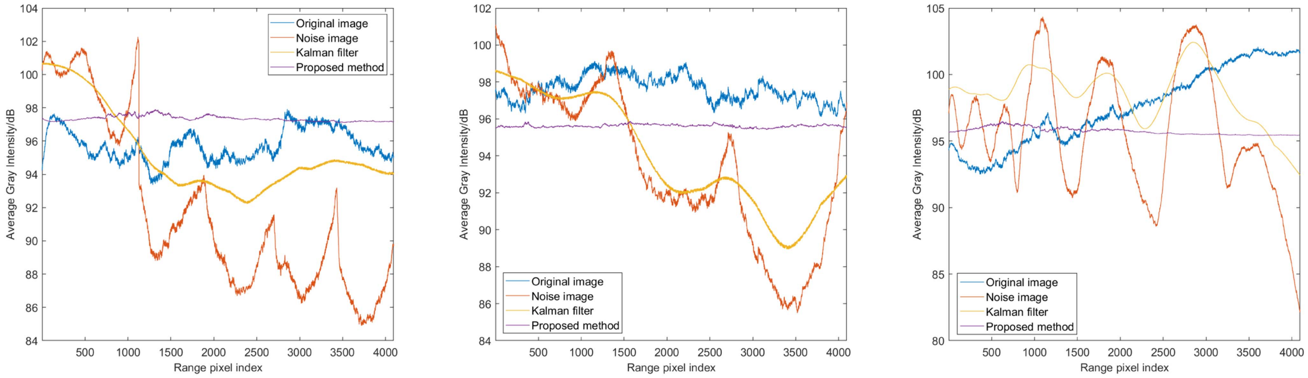

(a) (b) (c)

Fig. 13. AGI comparison of the simulated images. (a) IW. (b) EW. (c) ScanSAR.

TABLE I
QUALITY METRICS COMPARISON FOR THE SIMULATION EXPERIMENT

Quality metrics		SSIM	PSNR	DRF
Fig. 10	Kalman filter	0.979	23.821	2.491
	Proposed method	0.987	26.270	0.168
Fig. 11	Kalman filter	0.945	19.307	3.001
	Proposed method	0.984	24.514	0.079
Fig. 12	Kalman filter	0.919	18.777	2.131
	Proposed method	0.968	20.328	0.268

The SSIM is calculated by the formula

$$\mathrm{SSIM} = \frac{(2\bar{x}\bar{y} + c_1)(2\sigma_{xy} + c_2)}{(\bar{x}^2 + \bar{y}^2 + c_1)(\sigma_x^2 + \sigma_y^2 + c_2)} \tag{13}$$

where $\bar{x}$, $\bar{y}$, σ_x^2, σ_y^2, σ_{xy} are related to the mean, standard deviation and covariance of pixel intensities of images x and y, and c_1, c_2 are constants. A SSIM value closer to 1 indicates better structural similarity.

The PSNR is calculated by the formula

$$\mathrm{PSNR} = 10 \cdot \log_{10} \frac{(x_{\max})^2}{\mathrm{MSE}(x, y)} \tag{14}$$

where $x_{\max}$ is the maximum pixel value of the image. MSE(x,y), which stands for Mean Squared Error, is a measure calculated as the average of the squared differences between the pixel values of the image x and the image y over all pixels in the image. A higher PSNR value means better image quality. The results are given in Table I.

Figs. 10 and 11 show the processing results of the simulated EW and IW modes, respectively. The obvious scalloping effect and the step change between the subswaths can basically be removed after the method in [15]. However, comparing with the original image, it can be seen that there are still some light and dark variations in the range. After processing by the proposed method, the result is almost identical to the original image in terms of visual performance. Fig. 12 shows the processing results of the simulated ScanSAR mode. The image after the method in [15] still has significant shadow parts with the presence of residual scalloping, showing a visually performance poor. After processing by the proposed method, scalloping and ISB have been removed almost completely in the resultant image.

The AGI curves of the simulated images are shown in Fig. 13, where the blue curve represents the original image, the red curve represents the image after the addition of scalloping and ISB, and the yellow and purple ones are the results after the method in [15] and the proposed method, respectively. By comparing the curves, it can be seen that the method in [15] can only achieve ISB suppression in the local area, which is its limitation, and cannot solve the problem of energy inhomogeneity between subswaths. The proposed method suppresses ISB via global weighting and achieves energy equalization. Table I gives the quality metrics of the experimental results. Compared with the method in [15], the proposed one significantly improves the image quality. The result of the proposed method is the closest to the original image, which illustrates its effectiveness for ISB suppression. Notably, the purple curve corresponding to the image processed by the proposed method shows particular stability. Though not consistent with the original image's trend, it has little impact on subsequent processing, implying that this method only supports images with stable backgrounds like wide areas of land or ocean. In land-sea junction areas with drastic gray-level changes, it may not yield good results.

B. Scalloping and Interscan Banding Suppression of Real Images

In this section, four real SAR images with ISB are selected for processing, including both TOPS and ScanSAR modes. The blue curve represents the original image, the red curve represents the Kalman filter result and the yellow curve indicates the result by the proposed method. The MSI for Fig. 14(a) and (b) is 0.294, 0.423, respectively, which are smaller than the threshold 0.7

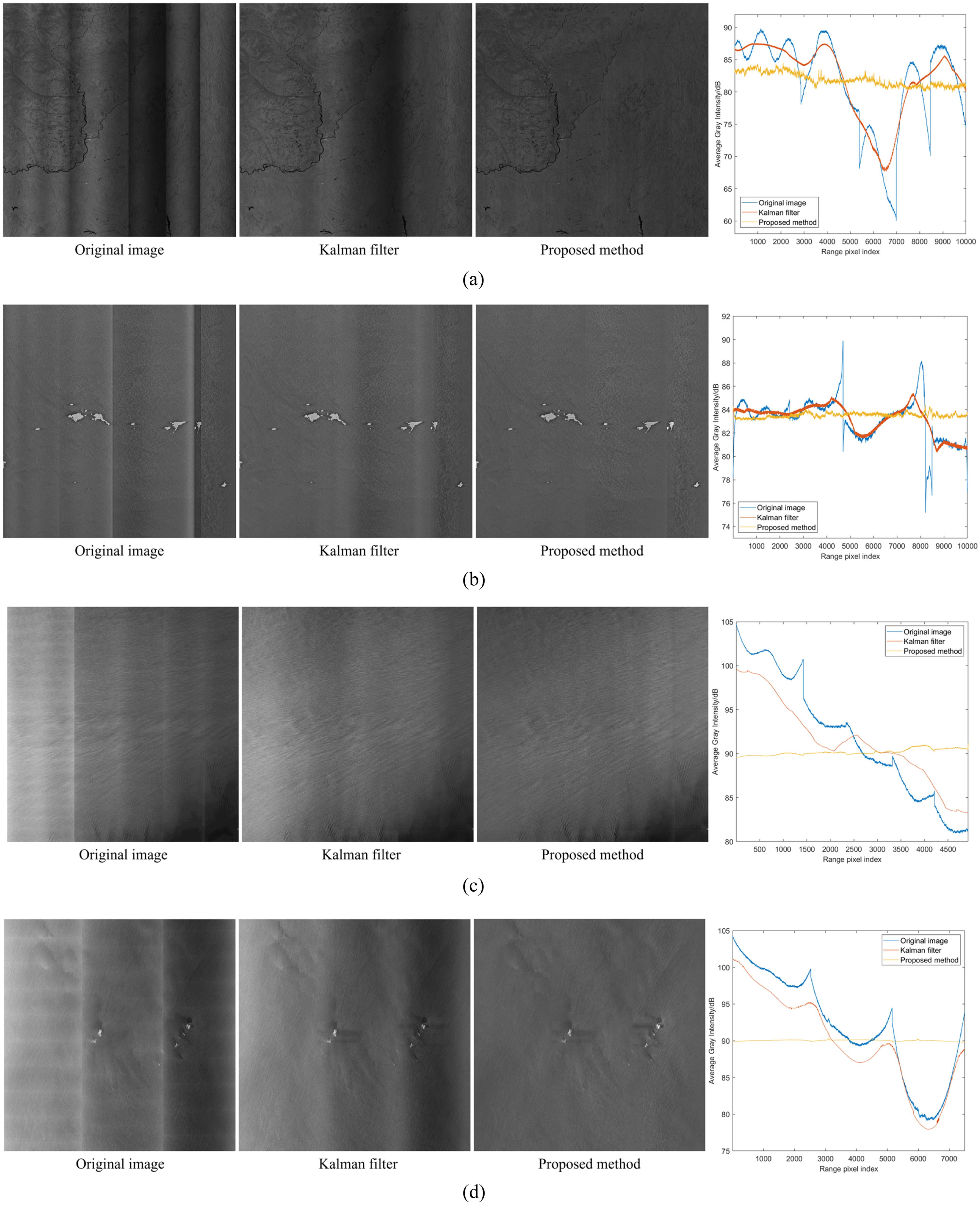

Fig. 14. Scalloping and interscan banding suppression results, where (a) and (b) are ScanSAR images, while (c) and (d) are TOPSAR images. (a) Data ID: GF3_MYC_WSC_031652_E126.4_N50.7_20220814_L1A_VHVV_L10006704187. (b) Data ID: GF3_MYC_WSC_034081_E124.8_N24.6_20230130_L1A_HHHV_L10006751573. (c) Data ID: S1A_EW_GRDM_1SDH_20170225T071535_20170225T071639_015437_019573_8318. (d) Data ID: S1A_IW_GRDH_1SDV_20240322T230504_20240322T230529_053101_066E8C_94C8.

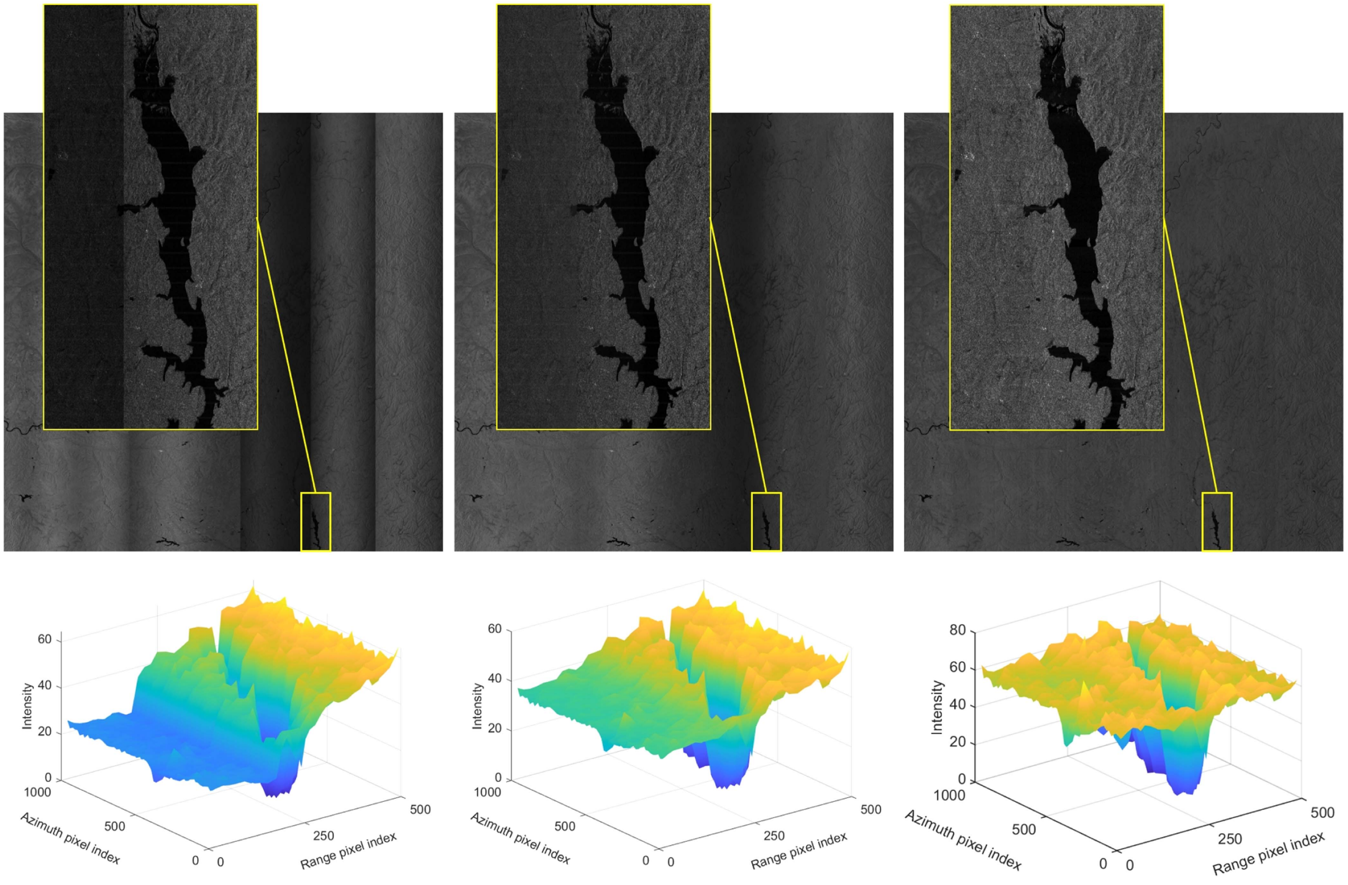

(a) (b) (c)

Fig. 15. Visual presentation (top) and energy map (bottom) of lake target from Fig. 14(a). (a) Original image. (b) Result of the method in [15]. (c) Result of the proposed method.

TABLE II
Degree of Range Fluctuation for the Images

	Original image	Kalman filter	Proposed method
Fig. 14(a)	7.032	5.641	1.029
Fig. 14(b)	1.774	1.604	0.194
Fig. 14(c)	6.873	4.587	0.337
Fig. 14(d)	6.996	6.435	0.085

and therefore require no scalloping suppression. The MSI for Fig. 14(c) and (d) is 0.751, 0.798, respectively; as they are larger than the threshold 0.7, scalloping suppression is needed. Table II gives the DRF of the image after suppression, and the data of the proposed method is better than the method in [15].

Fig. 14(a) shows the land scene of GF-3 in the ScanSAR mode. The original image has extremely strong and irregular ISB. In addition to the stepped state at the subswaths transition, the radiation intensity within each subswath has a large fluctuation amplitude, which is almost impossible to use in other applications. After suppressing ISB by the method in [15], the step state between subswaths is effectively eliminated. However, there is still an unreasonably shaded area in the image. In contrast, the proposed method restores the image to a good standarf, with shadows almost completely eliminated. The blue AGI curve has a very large amplitude change; the red one is a little smoother, but the overall amplitude change is also large; on the other hand, the yellow curve almost reaches a relatively flat state. This shows that the method is very effective in suppressing ISB and is consistent with image performance.

Fig. 14(b) shows the ocean scene of GF-3 in the ScanSAR mode. The ISB distribution in the original image is very uneven. The problem of subswath overlapping error can be found, which is a problem with the imaging process. Method in [15] eliminates the step line but the shadow part still exists, which is shown as unreasonable up and down fluctuations on the red AGI curve, while, the proposed method always maintains a very smooth amplitude with a much better performance.

Fig. 14(c) shows the ocean scene of Sentinel-1 in the EW mode, consisting of five subswaths. In addition to ISB, there is a relatively obvious scalloping effect in the image. Compared with the method in [15], the image processed by the proposed

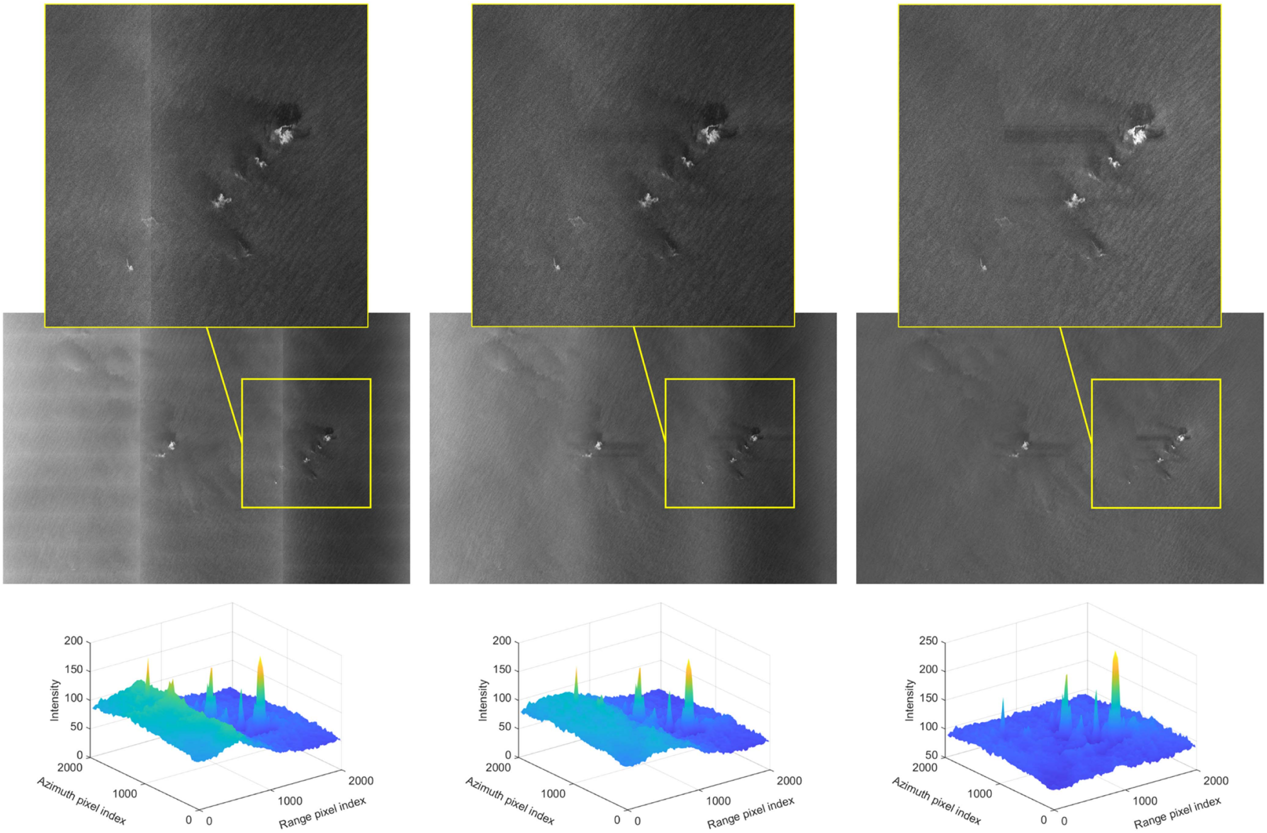

(a) (b) (c)

Fig. 16. Visual presentation (top) and energy map (bottom) of island target from Fig. 14(d). (a) Original image. (b) Result of the method in [15]. (c) Result of the proposed method.

method has clearer ocean texture information and more natural visual performance.

Fig. 14(d) shows the ocean scene of Sentinel-1 in IW mode, which consists of three subswaths. The scalloping width of this image is larger than that of Fig. 14(c). The image processed by method in [15] still has very obvious light and dark contrast areas. After processing by the proposed method, the shadow region in the image has been completely eliminated, which indicates that the proposed method achieves a good power compensation function result.

C. Further Performance Evaluation

In this section, the computational efficiency of the proposed method for ISB suppression and its ability to preserve target details are further examined.

First, the computational efficiency of both methods is analyzed. The proposed method is far more efficient than the method in [15], and this advantage becomes more apparent as the image gets larger. For an image of size $m \times n$, the method in [15] needs to compute the corresponding noise value separately for each pixel in the range. This is a continuous iterative computational process with a time complexity equivalent to $O(m \times n)$. The proposed method is a global weighting method, which does not require iterative loop operation, and the time complexity is equivalent to $O(m)$, where m is the number of range pixels, so this method is much more efficient. The computational efficiency of both methods is analyzed and presented in Table III. The proposed method is far more efficient than the method in [15], and this advantage becomes more apparent as the image gets larger. The programs used in this article are written on MATLAB, and the computer has twelve AMD Ryzen 9 7845HX CPUs (2.50 GHz) cores and 16 GB RAM.

TABLE III
ISB Suppression Processing Time by Different Methods

Image source	Image size	Processing time (s)	
		Kalman filter	Proposed method
Sentinel-1	4094 × 4094	54.28	0.84
GF-3	10 000 × 10 000	254.32	5.00

Second, two real SAR images are selected to analyze the target details, including the ScanSAR image from Fig. 14(a) and the TOPSAR image from Fig. 14(d).

Fig. 15 displays the target details of the ScanSAR image. Fig. 15(a) shows the land scene that is severely affected by ISB.

Although the selected lake target is not covered by ISB, the left side has severe intensity variations, which may affect the following processing tasks, such as detection and recognition of the lake target. After undergoing the method in [15], the situation has improved to some extent. However, the shaded portion of the adjacent region of the lake target remains relatively obvious, as shown in Fig. 15(b). In Fig. 15(c), the lake target and the neighboring region have been restored to the status of a normal image after being processed by the proposed method. By observing the energy change in the region, it is evident that the lake target remains almost unaffected after being processed by the present method, and the energy in the region near the lake target reaches a consistent level without loss of detailed information.

Fig. 16 displays the target details of the TOPSAR image. The target in the image is floating ice in the ocean scene. After applying the method in [15], there is no significant change in the intensity of the target or nearby regions. However, after implementing the proposed method, the shadow areas are suppressed and the intensity of the target is enhanced, resulting in greater distinction within the scene. All these demonstrate the excellent ability of the proposed method in preserving image details.

IV. CONCLUSION

In this article, the issue of ISB in ScanSAR and TOPSAR images has been thoroughly investigated. Subsequently, an ISB suppression method founded on the Retinex theory and global weighting has been proposed. By integrating with prior research findings, a combined and comprehensive approach for suppressing both ISB and scalloping has been developed.

The superiority of the proposed method is manifested in three key aspects. First, it can effectively mitigate ISB and scalloping in SAR images without the need for any supplementary information, enhancing its practical applicability. Second, it exhibits robustness and consistently good performance across diverse images, eliminating the necessity for parameter tuning, which simplifies its implementation. Third, it demonstrates high efficiency and is particularly adept at processing large-sized images, thereby meeting the requirements of handling massive data. These advantages have been rigorously validated through the processing of both simulated and real SAR images.

However, it should be noted that the current method has been primarily designed and tested under relatively simple and homogeneous SAR image backgrounds. In complex environments, such as sea-land boundaries and areas with highly intricate scattering conditions, the method may face limitations. This is because at sea-land boundaries, the global weighting method is subject to interference from the mixture of sea and land backscattering characteristics. In regions with complex scattering elements, the highly variable scattering mechanisms also conflict with the assumptions of the proposed method. Therefore, in future research, we plan to address the impacts of the above factors on the proposed method by integrating various segmentation algorithms and explore its adaptability and potential in more scenarios and tasks, such as ship detection, sea ice detection, etc.

REFERENCES

[1] A. Moreira, P. Prats-Iraola, M. Younis, G. Krieger, I. Hajnsek, and K. P. Papathanassiou, "A tutorial on synthetic aperture radar," *IEEE Geosci. Remote Sens. Mag.*, vol. 1, no. 1, pp. 6–43, Mar. 2013.

[2] F. De Zan and A. Monti Guarnieri, "TOPSAR: Terrain observation by progressive scans," *IEEE Trans. Geosci. Remote Sens.*, vol. 44, no. 9, pp. 2352–2360, Sep. 2006.

[3] J.-W. Park, A. A. Korosov, M. Babiker, S. Sandven, and J.-S. Won, "Efficient thermal noise removal for Sentinel-1 TOPSAR cross-polarization channel," *IEEE Trans. Geosci. Remote Sens.*, vol. 56, no. 3, pp. 1555–1565, Mar. 2018.

[4] J. Karvonen, "Baltic sea ice concentration estimation using SENTINEL-1 SAR and AMSR2 microwave radiometer data," *IEEE Trans. Geosci. Remote Sens.*, vol. 55, no. 5, pp. 2871–2883, May 2017.

[5] K. Zhang, B. Zhang, W. Perrie, G. Zheng, J. Yang, and H. Fang, "Assessment of thermal noise effect on wind speed retrieval accuracy using Sentinel-1 cross-polarized TOPSAR images," *IEEE Trans. Geosci. Remote Sens.*, vol. 61, 2023, Art. no. 4208011.

[6] X. Wang, C. Chen, Z. Pan, and Z. Pan, "Superpixel-based LCM detector for faint ships hidden in strong noise background SAR imagery," *IEEE Geosci. Remote Sens. Lett.*, vol. 16, no. 3, pp. 417–421, Mar. 2019.

[7] Y. Zhu, J. Ai, L. Wu, D. Guo, W. Jia, and R. Hong, "An active multi-target domain adaptation strategy: Progressive class prototype rectification," *IEEE Trans. Multimedia*, to be published, doi: 10.1109/TMM.2024.3521740.

[8] J. Ai et al., "AIS-PVT: Long-time AIS data assisted pyramid vision transformer for sea-land segmentation in dual-polarization SAR imagery," *IEEE Trans. Geosci. Remote Sens.*, vol. 62, 2024, Art. no. 5220712, doi: 10.1109/TGRS.2024.3449894.

[9] J. Ai, Y. Mao, Q. Luo, L. Jia, and M. Xing, "SAR target classification using the multikernel-size feature fusion-based convolutional neural network," *IEEE Trans. Geosci. Remote Sens.*, vol. 60, 2022, Art. no. 5214313, doi: 10.1109/TGRS.2021.3106915.

[10] D. Wang, Y. Song, J. Huang, D. An, and L. Chen, "SAR target classification based on multiscale attention super-class network," *IEEE J. Sel. Top. Appl. Earth Observ. Remote Sens.*, vol. 15, pp. 9004–9019, 2022, doi: 10.1109/JSTARS.2022.3206901.

[11] "Sentinel-1 product specification, document S1-RS-MDA-52- 7441," Issue 3/3, 2016. [Online]. Available: https://sentinel.esa.int/documents/247904/349449/Sentinel-1_Product_Specification

[12] A. Korosov, D. Demchev, N. Miranda, N. Franceschi, and J.-W. Park, "Thermal denoising of cross-polarized Sentinel-1 data in interferometric and extra wide swath modes," *IEEE Trans. Geosci. Remote Sens.*, vol. 60, 2022, Art. no. 5218411.

[13] P. Q. Lee, L. Xu, and D. A. Clausi, "Sentinel-1 additive noise removal from cross-polarization extra-wide TOPSAR with dynamic leastsquares," *Remote Sens. Environ.*, vol. 248, 2020, Art. no. 111982.

[14] P. Q. Lee, L. Xu, and D. A. Clausi, "Estimating noise floor in Sentinel-1 images with linear programming and least squares," *IEEE Trans. Geosci. Remote Sens.*, vol. 60, 2022, Art. no. 5212414.

[15] M. Iqbal and J. Chen, "Removal of scalloping in ScanSAR images using Kalman filter," in *Proc. IEEE Int. Geosci. Remote Sens. Symp.*, 2012, pp. 260–263, doi: 10.1109/IGARSS.2012.6351588.

[16] G. Xinwei et al., "Suppression of scalloping and inter-scan banding in non-stationary ScanSAR images based on Kalman filter and image segmentation," *J. Nav. Aeronaut. Astron. Univ.*, vol. 132, no. 5, pp. 125–129, Dec. 2017.

[17] W. Yang, Y. Li, W. Liu, J. Chen, C. Li, and Z. Men, "Scalloping suppression for ScanSAR images based on modified Kalman filter with preprocessing," *IEEE Trans. Geosci. Remote Sens.*, vol. 59, no. 9, pp. 7535–7546, Sep. 2021.

[18] W. Yang et al., "An adaptive scalloping suppression method for ScanSAR images based on the Kalman filter," *IEEE Trans. Geosci. Remote Sens.*, vol. 62, 2024, Art. no. 5205613.

[19] A. Meta, P. Prats, U. Steinbrecher, J. Mittermayer, and R. Scheiber, "TerraSAR-X TOPSAR and ScanSAR comparison," in *Proc. 7th Eur. Conf. Synthetic Aperture Radar*, 2008, pp. 1–4.

[20] A. Meta, J. Mittermayer, P. Prats, R. Scheiber, and U. Steinbrecher, "TOPS imaging with TerraSAR-X: Mode design and performance analysis," *IEEE Trans. Geosci. Remote Sens.*, vol. 48, no. 2, pp. 759–769, Feb. 2010.

[21] S. Wollstadt, P. Prats, M. Bachmann, J. Mittermayer, and R. Scheiber, "Scalloping correction in TOPS imaging mode SAR data," *IEEE Geosci. Remote Sens. Lett.*, vol. 9, no. 4, pp. 614–618, Jul. 2012.

[22] X. Zhang, S. Liu, H. Yu, X. Tong, and G. Huang, "Effect of antenna pointing errors on SAR imaging considering the change of the point target location," *ISPRS Ann. Photogramm., Remote Sens. Spatial Inf. Sci.*, vol. 3, pp. 267–271, Apr. 2018.

[23] I. G. Cumming and D. C. Bast, "A new hybrid-beam data acquisition strategy to support ScanSAR radiometric calibration," *IEEE Trans. Geosci. Remote Sens.*, vol. 42, no. 1, pp. 3–13, Jan. 2004.

[24] S. Lim, I. Choi, and T. Jeong, "Compensation method for a wideband signal's squint problem of an AESA SAR system using a cross-range-variant antenna gain equalizer," *IEEE Sensors J.*, vol. 19, no. 8, pp. 2937–2945, Apr. 2019.

[25] Y. Wang, C. Liu, R. Zhu, M. Liu, Z. Ding, and T. Zeng, "MAda-Net: Model-adaptive deep learning imaging for SAR tomography," *IEEE Trans. Geosci. Remote Sens.*, vol. 61, 2023, Art. no. 5202413.

[26] Z. Chen, H. Zeng, W. Yang, and J. Chen, "Texture enhancement method of oceanic internal waves in SAR images based on non-local mean filtering and multi-scale retinex," in *Proc. 3rd China Int. SAR Symp.*, 2022, pp. 1–5.

Xinwei An (Graduate Student Member, IEEE) was born in 2001. He received the B.E. degree in communication engineering from the University of Electronic Science and technology of China, Chengdu, China, in 2022. He is currently working toward the Ph.D. degree in signal and information processing with the School of Electronic Information Engineering, Beihang University, Beijing, China.

His research interests include spaceborne synthetic aperture radar image quality improvement and intelligent interpretation.

Wei Yang (Member, IEEE) was born in 1983. He received the M.S. and Ph.D. degrees in signal and information processing from Beihang University (BUAA), Beijing, China, in 2008 and 2011, respectively.

From 2011 to 2013, he was a Postdoctoral with the School of Electronics and Information Engineering, BUAA, where he has been a Lecturer with the School of Electronics and Information Engineering since 2013. From 2016 to 2017, he was a Visiting Researcher with the Department of Electronic and Electrical Engineering, The University of Sheffield, Sheffield, U.K. He has been an Associate Professor with the School of Electronics and Information Engineering, BUAA, since 2018, and a Professor since 2023. He has authored or coauthored more than 60 journals and conference publications. His research interests include moving target detection, high-resolution spaceborne synthetic aperture radar (SAR) image formation, SAR image quality improvement, and 3-D imaging.

Haijun Shen was born in September 1987. He received the master's degree in engineering from the Shanghai Academy of Spaceflight Technology, Shanghai, China, in 2012.

He is currently engaged in the overall design of satellites at the Shanghai Institute of Satellite Engineering.

Hongcheng Zeng (Member, IEEE) was born in 1989. He received the Ph.D. degree in signal and information processing from Beihang University, Beijing, China, in 2016.

From 2016 to 2019, he was a Postdoctoral with the School of Electronics and Information Engineering, Beihang University, where he has been an Assistant Professor since August 2019. He was a Visiting Researcher with the School of Mathematics and Statistics, The University of Sheffield, Sheffield, U.K., from 2017 to 2018. Since 2022, he has been an Associate Professor with the School of Electronics and Information Engineering, Beihang University. He has authored or coauthored more than 40 journal and conference publications. His research interests include SAR target detection, high-resolution spaceborne SAR image formation and passive radar signal processing.

Fei Zou received the Ph.D. degree in information and communication engineering from the National University of Defense Technology, Changsha, China, in 2012.

Since 2017, she has been an Associate Researcher with the Beijing Institute of Remote Sensing Informatin, Beijing, China. She has published more than ten journal and conference papers. Her research interests include inverse SAR imaging, SAR image quality improving, and remote sensing application.

Jiadong Deng (Graduate Student Member, IEEE) was born in 1995. He received the B.S. degree in information and computational science in 2017 from Beihang University, Beijing, China, where he is currently working toward the Ph.D. degree in signal and information processing.

His research interests include spaceborne synthetic aperture radar image formation for terrain observation by progressive scans mode and sliding spotlight mode.

Can Su (Graduate Student Member, IEEE) was born in 1998. He received the bachelor's degree in electronic information engineering from Beihang University, Beijing, China, in 2020. He is currently working toward the Ph.D. degree in signal and information processing with the School of Electronic Information Engineering, Beihang University, Beijing, China.

His research direction is remote sensing intelligent interpretation algorithms based on AI technology, specifically in intelligent target detection, target recognition, and target behavior prediction analysis of spaceborne SAR data.

Wei Liu (Senior Member, IEEE) received the B.Sc. degree in space physics and the LL.B. degree in intellectual property law from Peking University, Beijing, China, in 1996 and 1997, respectively, the M.Phil. degree from the Department of Electrical and Electronic Engineering, The University of Hong Kong, Hong Kong, in 2001, and the Ph.D. degree from the School of Electronics and Computer Science, University of Southampton, Southampton, U.K., in 2003.

He was a Postdoctoral with the University of Southampton and also with Imperial College London, London, U.K. From 2005 to 2023, he was a Lecturer and a Senior Lecturer with the Department of Electronic and Electrical Engineering, University of Sheffield, Sheffield, U.K. From 2023 to 2024, he was a Reader with the School of Electronic Engineering and Computer Science, Queen Mary University of London, London. Since 2024, he has been a Professor with the Department of Electrical and Electronic Engineering, The Hong Kong Polytechnic University, Hong Kong. He has authored or coauthored more than 430 journal articles and conference papers, six book chapters, and two research monographs titled "*Wideband Beamforming: Concepts and Techniques*" (Wiley, 2010) and "*Low-Cost Smart Antennas*" (Wiley, 2019), respectively. His research interests cover a wide range of topics in signal processing, with a focus on sensor array signal processing and its various applications, such as robotics and autonomous systems, human–computer interface, radar, sonar, and wireless communications.

Dr. Liu is a Member of the Applied Signal Processing Systems Technical Committee of the IEEE Signal Processing Society for the term 2023–2025. He was the Chair of the Sensor Array and Multichannel Signal Processing Technical Committee of the IEEE SPS, from 2021 to 2022 and the Digital Signal Processing Technical Committee of the IEEE Circuits and Systems Society, from 2022 to 2024 and is the Chair of the IEEE SPS Education Board of its Educational Conference Program Committee for the term 2024–2026. He was a Member of the Sensor Array and Multichannel Signal Processing Technical Committee of the IEEE SPS from 2021 to 2022, the IEEE SPS Technical Directions Board from 2021 to 2022, and the IEEE SPS Conference Board and its Executive Subcommittee from 2022 to 2023. He was an Associate Editor for IEEE Transactions on Signal Processing, IEEE Access, and *Journal of the Franklin Institute.* He is currently an Associate Editor for IEEE Antennas and Wireless Propagation Letters and an Executive Associate Editor-in-Chief for *Frontiers of Information Technology* and *Electronic Engineering*. He was an IEEE Distinguished Lecturer for the Aerospace and Electronic Systems Society, from 2023 to 2024.